Biosensors and Bioelectronics 301 (2026) 118490

Contents lists available at ScienceDirect

Biosensors and Bioelectronics

journal homepage: www.elsevier.com/locate/bios

In situ mapping of HSA reabsorption by a NIR fluorogenic sensor as a practical phenotypic assay for nephroprotective drug discovery

Yufan Fan [a,b,1], Bei Zhao [b,1], Ya Zhang [c,1], Pingjin Xie [d], Lele Liu [b], Xuerui Wang [b], Guanghao Zhu [b], Zhaobin Guo [a,b], Fangyuan Wang [b,****], Qiang Jin [a,b,***], Jing Hu [a,**], Guangbo Ge [b,e,*]

[a] *Department of Nephrology, The Seventh People's Hospital of Shanghai University of Traditional Chinese Medicine, Shanghai, 200137, China*
[b] *State Key Laboratory of Discovery and Utilization of Functional Components in Traditional Chinese Medicine, Shanghai Frontiers Science Center of TCM Chemical Biology, Institute of Interdisciplinary Integrative Medicine Research, Shanghai University of Traditional Chinese Medicine, Shanghai, 201203, China*
[c] *Department of Pharmacy, Jingan District Zhabei Central Hospital, Shanghai, 200070, China*
[d] *Shenzhen Hospital of Shanghai University of Traditional Chinese Medicine, Shanghai, 201203, China*
[e] *School of Pharmacy, Yichun University, Yichun, 336000, China*

ARTICLE INFO

Keywords:
Human serum albumin (HSA)
Ligand-based probe design
Albumin endocytosis
Nephroprotective agents

ABSTRACT

The impaired reabsorption of kidney tubules is a critical early event in drug-induced kidney injury (DIKI), making real-time monitoring of human serum albumin (HSA) endocytosis essential for assessing renal function and screening nephroprotective agents. Inspired by the specific warfarin-HSA interactions, a novel coumarin-derived near-infrared (NIR) fluorogenic sensor, **NCBP**, was engineered based on a twisted intramolecular charge transfer (TICT) mechanism. Under physiological conditions, **NCBP** rapidly and stably bound to subdomain IIA of HSA with 1:1 stoichiometry, triggering a 79-fold fluorescence enhancement at 665 nm. **NCBP** integrated multiple advantages for detecting HSA, including instantaneous response, high physicochemical stability, ultrahigh sensitivity, and excellent selectivity. Furthermore, **NCBP** enabled *in situ* spatiotemporal imaging of HSA reabsorption in living nephrocytes and renal tissues, which was then used for screening nephroprotective agents to mitigate cisplatin-induced nephrotoxicity (CINT). Nobiletin (NOB) and 4',7-dimethoxyisoflavone (DIF) were identified as promising lead compounds capable of restoring renal uptake function and mitigating cisplatin-induced oxidative stress. In CINT mice, both NOB and DIF significantly improved renal function and attenuated tubular injury, confirming their nephroprotective potentials. Collectively, a TICT-based NIR sensor was developed for *in situ* imaging of HSA reabsorption, offering a robust phenotypic platform for spatiotemporal mapping of cellular HSA trafficking and discovering nephroprotective agents.

1. Introduction

Acute kidney injury (AKI), characterized by a sudden decline in renal function, imposes a heavy burden on healthcare systems worldwide due to its high incidence and poor prognosis. Drug-induced nephrotoxicity is a leading cause of AKI, with the chemotherapeutic agent cisplatin (CDDP) serving as a typical example (Yang et al., 2025). CDDP triggers a cascade of intracellular stresses, including DNA damage, mitochondrial

---

[*] Corresponding authors. State Key Laboratory of Discovery and Utilization of Functional Components in Traditional Chinese Medicine, Shanghai Frontiers Science Center of TCM Chemical Biology, Institute of Interdisciplinary Integrative Medicine Research, Shanghai University of Traditional Chinese Medicine, Shanghai, 201203, China.

[**] Corresponding author. Department of Nephrology, The Seventh People's Hospital of Shanghai University of Traditional Chinese Medicine, Shanghai, 200137, China.

[***] Corresponding author. Department of Nephrology, The Seventh People's Hospital of Shanghai University of Traditional Chinese Medicine, Shanghai, 200137, China.

[****] Corresponding author.

E-mail addresses: wangfangyuan@zcmu.edu.cn (F. Wang), jindicp@163.com (Q. Jin), hujing@shutcm.edu.cn (J. Hu), geguangbo@shutcm.edu.cn (G. Ge).

[1] These authors contributed equally to this work.

https://doi.org/10.1016/j.bios.2026.118490
Received 31 December 2025; Received in revised form 31 January 2026; Accepted 4 February 2026

dysfunction, and oxidative stress, thereby compromising the structural and functional integrity of renal tubular epithelial cells, particularly in the proximal tubule (Malik et al., 2015; Tang et al., 2023). Consequently, these injuries manifest as measurable changes in specific pharmacological phenotypes, such as elevated levels of tubular stress markers (e.g., TIMP-2, IGFBP-7), direct injury biomarkers (e.g., KIM-1, NGAL), and pro-inflammatory cytokines (e.g., IL-18) (Strauss et al., 2024; Wen and Parikh, 2021). Besides, the capacity of the proximal tubule to reabsorb filtered proteins such as human serum albumin (HSA) is also a critical indicator of renal health and a sensitive biomarker of early-stage kidney injury. Real-time monitoring of HSA reabsorption in renal tubular cells is a valuable approach for assessing drug-induced nephrotoxicity and identifying potential nephroprotective agents.

As the most abundant plasma protein (35–55 g/L in healthy individuals), HSA has been recognized as a significant biomarker for diverse pathological conditions, such as hepatic dysfunction, nephrotic syndrome, and renal injury (Arques, 2018; Carvalho and Verdelho Machado, 2018). Although bromocresol green (BCG) method has been used for HSA quantification for decades, its utility remains constrained by insufficient detection sensitivity and an inability to dynamically track HSA in native biological environments (Kumar and Banerjee, 2017; Xu et al., 2022). Fluorogenic probes have emerged as powerful tools for decoding the activity dynamics or expression level of target proteins, with the merits of high sensitivity, high throughput, and *in-situ* visualization (Fan et al., 2025; Fan et al., 2023c; Niu et al., 2026; Niu et al., 2025). Currently, HSA probes are categorized into activity-based probes (ABPs) and binding-based probes (BBPs) (Kim et al., 2013; Xing et al., 2020). ABPs exploit the weak *pseudo*-esterase activity of HSA for selective recognition but are hampered by prolonged incubation period and suboptimal detection limitation (>2.5 μg/mL) (Ge et al., 2017; Jin et al., 2017). In contrast, BBPs capitalize on the powerful ligand-capturing ability of hydrophobic pockets in HSA, enabling rapid response, ultrahigh sensitivity, and reversible labeling (Fan et al., 2023a). Strategic molecular engineering of BBP fluorophores, based on mechanisms such as twisted intramolecular charge transfer (TICT), aggregation-induced emission (AIE), and excited-state intramolecular proton transfer (ESIPT), allows programmable fluorescence switching (Gao et al., 2023; Gu et al., 2023; Tu et al., 2019; Wang et al., 2017). These environment-sensitive dyes display faint fluorescence in aqueous media but undergo substantial signal amplification upon binding to HSA through conformational restriction or stabilization of keto-enol tautomerization states (Fan et al., 2025; Sedgwick et al., 2018).

Most reported BBPs still face several limitations, including short emission wavelengths, low quantum yields, poor signal-to-noise ratio (SNR), and insufficient sensitivity (Table S1). These intrinsic drawbacks hinder highly sensitive tracking of HSA in biological milieus. While near-infrared (NIR) sensors (>650 nm) offer enhanced anti-interference capability and superior spatiotemporal resolution, few existing NIR sensors simultaneously satisfy the dual criteria of optimal spectral performance and specific molecular recognition (Song et al. 2024, 2025). Moreover, high binding affinity of BBPs toward HSA is essential for specific target recognition and stable complex formation, which in turn improves detection accuracy and optical signal stability (Gao et al., 2019; Zhu et al., 2024). An ideal HSA-binding sensor should emit within the biological optical window, demonstrating high affinity, exceptional specificity, rapid response, high SNR, considerable quantum yield, and robust stability. Therefore, the development of such optimized NIR sensors integrating strong HSA binding with intense fluorescence output is crucial for achieving high-contrast imaging of HSA-related biological processes.

Herein, a drug-inspired sensor design strategy was adopted to construct a NIR fluorogenic tool for *in-situ* spatiotemporal mapping of HSA reabsorption in living systems. Inspired by the high binding affinity of warfarin for HSA, a library of TICT-based 7-diethylaminocoumarin dyes was rationally constructed. Through combining structure-based virtual screening and experimental validation, the fluorogenic sensor (*E*)-4-(2-(7-(diethylamino)-2-oxo-2*H*-chromen-3-yl) vinyl)-1-ethylquinolin-1-ium iodide (**NCBP**) was identified as an optimal candidate, owing to its excellent photophysical properties and remarkable SNR. Upon addition of HSA, **NCBP** was rapidly captured by HSA to form a stable complex that emitted intensive fluorescent signals around 665 nm. Next, the sensing performance, detection sensitivity, and binding mechanism of **NCBP** toward HSA were systematically investigated. Finally, the utility of **NCBP** in the assessment of uptake capacity of renal tubular cells and the discovery of nephroprotective drugs, were demonstrated.

2. Experimental section

2.1. *Structure-based virtual screening*

Eight crystal structures of HSA (PDB ID: 1AO6, 1BM0, 1E78, 2BXD, 2VUF, 4K2C, 6M4R, and 7DJN) were downloaded from the Protein Data Bank. AutoDock Vina performed molecular docking simulations. According to a standard protocol, the PDBQT files for eight receptors were prepared by deleting water molecules and redundant heteroatoms, adding the polar hydrogens, adding Kollman charges, and assigning AD4 type. All probes were submitted to AutoDock Tools using default parameters after energy minimization. A grid box wrapped the entire albumin.

2.2. *In situ imaging of HSA reabsorption in nephrocytes*

Renal tubular epithelial cell lines (RPTEC/TERT1 and HK-2) were maintained in DMEM high-glucose medium supplemented with 10% fetal bovine serum (FBS), penicillin (100 U/mL), and streptomycin (100 μg/mL) at 37 °C in a 5% CO_2 atmosphere. Upon reaching approximately 80% confluency, cells were detached and seeded into 24-well plates at a density of 1×10^4 cells per well. Following overnight attachment, the model group was exposed to cisplatin (CDDP, 3 μM), whereas treatment groups were pre-treated with sulforaphane (SFN, 5 and 20 μM) for 2 h prior to the addition of CDDP (3 μM); all groups were then co-incubated for 24 h. After discarding the supernatant, cells were washed twice with phosphate-buffered saline (PBS) and incubated in serum-free medium for an additional 12 h. The medium was then aspirated, and cells were washed once with PBS. Subsequently, cells were stained with both the probe **NCBP** (200 nM) and the reactive oxygen species (ROS) probe DCFH-DA (10 μM) for 30 min. After removal of the probe solutions, cells were washed twice with PBS. One subset of cells was further incubated with albumin, while a blank control group received PBS instead. After incubation, the supernatant was aspirated and replaced with PBS. Fluorescence imaging was performed using an inverted fluorescence microscope.

2.3. *Screening of nephroprotective drugs*

RPTEC cells were seeded at a density of 2×10^4 cells per well in DMEM medium supplemented with 10% FBS and cultured overnight. Following pretreatment with the candidate drug (10 μM) for 2 h, the cells were exposed to CDDP (10 μM) for 24 h. After removal of the supernatant, cells were incubated with the **NCBP**-albumin complex (200 nM) for 1 h. Subsequently, the supernatant was aspirated, and cells were washed three times with PBS. Finally, the cells were maintained in PBS and analyzed using a microplate reader with excitation and emission wavelengths set at 520 nm and 665 nm, respectively.

2.4. *Experimental animal protocols*

All experimental protocols involving animals were performed in compliance with the institutional ethical guidelines (Shanghai University of Traditional Chinese Medicine Animal Care Committee Approval No. PZSHUTCM2311130003) and in accordance with the National Institutes of Health Guide for the Care and Use of Laboratory Animals.

Male C57BL/6J mice (8–10 weeks old) were procured from Shanghai Jihui. After a one-week acclimatization period, male mice were randomly assigned to six groups (n = 6 per group): control group, cisplatin group (CDDP), CDDP + NOB low-dose group (NOB, 20 mg/kg), CDDP + NOB high-dose group (NOB, 40 mg/kg), CDDP + DIF low-dose group (DIF, 20 mg/kg), and CDDP + DIF high-dose group (DIF, 40 mg/kg). NOB or DIF was administered intraperitoneally once daily at the indicated doses for a total duration of 6 d. Drug administration was initiated 3 d prior to cisplatin challenge. At 3 d, acute renal injury was induced by a single intraperitoneal injection of CDDP (25 mg/kg) in all CDDP-treated groups, while control mice received an equal volume of vehicle. NOB or DIF administration was continued once daily for an additional 3 d following cisplatin exposure. At 6 d, mice were euthanized, and blood and kidney tissues were collected for subsequent biochemical and histological analysis.

3. Results and discussion

3.1. Rational design of TICT-based NIR sensors for HSA

In the native state, HSA resembles a heart-shaped asymmetric structure, with high affinity for various endogenous ligands and clinical drugs (Scheme 1A). Warfarin, a common anticoagulant agent, exhibits high HSA binding rate (~99%) and binding affinity ($K_d = 4.68\ \mu\text{M}$) (Ufer, 2005). An in-depth interaction analysis of the warfarin-HSA complex (PDB ID: 2BXD) revealed that the coumarin ring formed multiple hydrogen bonds and hydrophobic interactions with HSA (Scheme 1B and Fig. S1) (Ghuman et al., 2005). Building on this finding, a drug ligand-driven molecular engineering strategy was proposed to construct high-performance BBPs for HSA (Scheme 1C). Coumarin was retained as the fluorogenic scaffold due to its inherent affinity for HSA, along with tunable emission, high quantum yield, good biocompatibility, and environmental sensitivity (Fan et al., 2023b; Liu et al., 2025). Systematic structure-property optimization of coumarin dyes was achieved by introducing an electron-donating *N*, *N*-diethylamino group at the 7-position and a π-bridge unit at the 3-position that connects a potent electron-acceptor unit, resulting in an enhanced push-pull configuration (Chen et al., 2020; Guo et al., 2019; Sun et al., 2023). This dual-rotor architecture promoted efficient TICT formation in aqueous media, effectively suppressing background fluorescence and improving the SNR (Fu et al., 2021; Wang et al., 2023; Yang et al., 2020). Upon binding with HSA's hydrophobic sites, the flexible intramolecular rotation of TICT dyes would be totally restricted, leading to remarkable fluorescence enhancement (Wang et al., 2021).

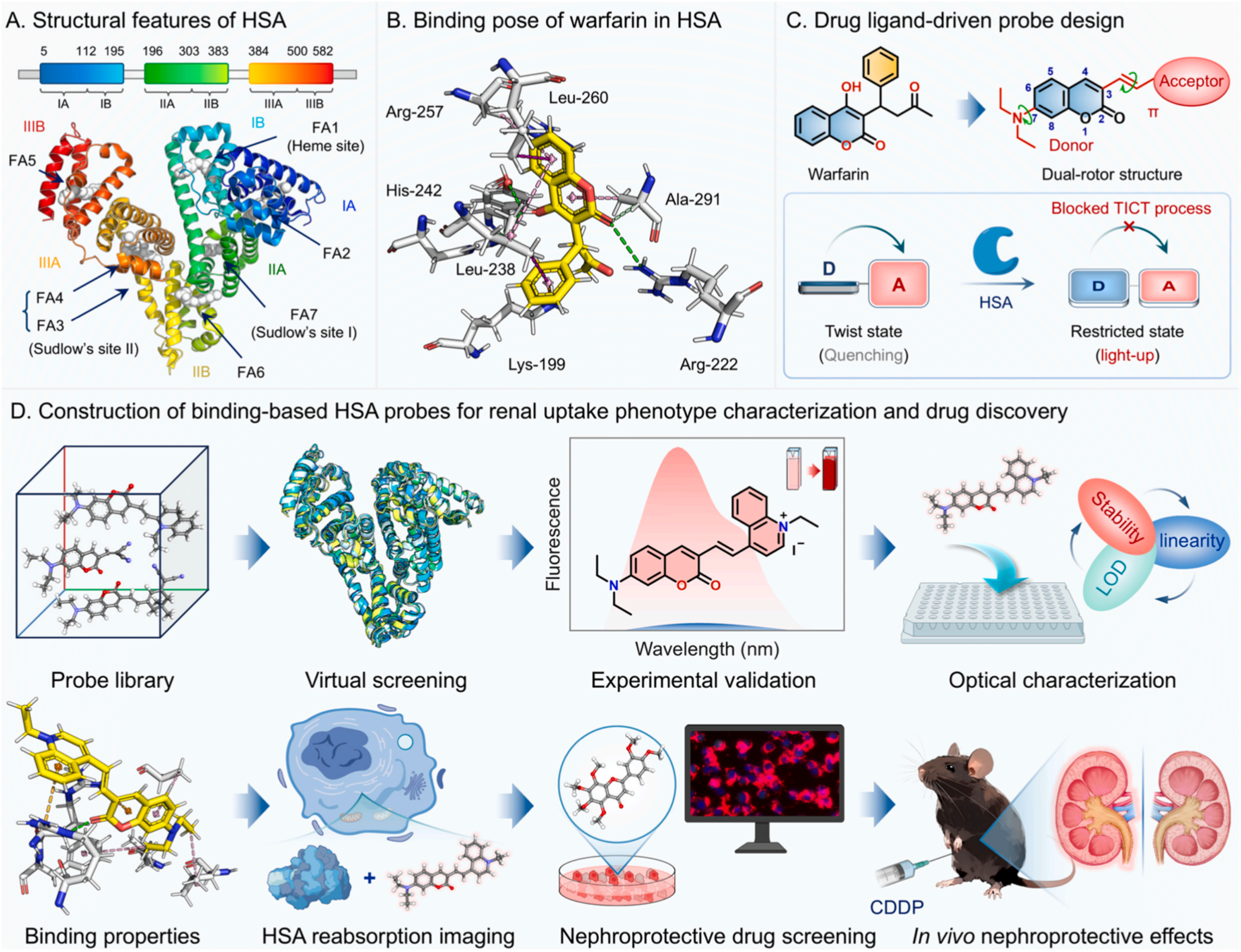

Scheme 1. Rational engineering of HSA sensors based on a drug-inspired engineering strategy. (A) Structural features and drug-binding sites of HSA. (B) Binding mode of warfarin in subdomain IIA of HSA (PDB ID: 2BXD). (C) Sensing mechanism of TICT-based coumarin dyes for HSA. (D) Cascade screening, performance characterization, and biological applications of **NCBP**.

3.2. Dual screening of high-performance HSA sensors

As a proof of concept, a library of 7-diethylaminocoumarin dyes featuring a donor-π-acceptor (D-π-A) architecture was constructed (Fig. S2) (Fan et al., 2023b). High-performance HSA sensors were subsequently identified through an integrated approach combining computer-aided virtual screening and spectroscopic validation (Scheme 1D). First, the plasma protein-binding rates of fourteen candidate sensors were assessed using ADMETlab. All designed derivatives exhibited binding rates exceeding 95% (Fig. 1A). In parallel, ensemble docking simulations were employed to quantify the binding affinity of each sensor toward HSA. Given the conformational flexibility of the HSA binding cavity, eight crystal structures of HSA (PDB IDs: 1AO6, 1BM0, 1E78, 2BXD, 2VUF, 4K2C, 6M4R, 7DJN) were retrieved and docked individually with each ligand (Table S2). These dyes uniformly exhibited favorable affinity for HSA, with predicted binding energies below −8 kcal/mol (Fig. 1B). Sensors 2, 3, 5, 8, 9, and 11 showed particularly strong binding. Since the malononitrile moiety in sensor 1 had also been reported to bind HSA, these seven sensors were synthesized for further experimental evaluation (Fig. 1C and Scheme S1–7 and Figs. S3–22). Next, fluorescence titration experiments were conducted to investigate signal variations upon HSA binding. Compared with the free sensor, sensors 1, 3, 5, and 9 elicited over 50-fold signal enhancement upon addition of HSA (Fig. 1D and Fig. S23). Although sensor 1 exhibited the most pronounced fluorescence increase upon HSA binding, it was excluded from subsequent studies owing to its limited emission wavelength, which makes it susceptible to interference from biological matrices. In terms of the emission wavelength and fluorescence changes, the sensing performance of sensor 9 (i.e., **NCBP**) was superior to that of sensors 3 and 5. **NCBP** showed relatively weak fluorescence ($\Phi_{fl} = 0.025$) in aqueous buffer due to the TICT effect (Fig. 1E and Table S3). In the presence of HSA, the fluorescence intensity around 665 nm increased up to 79 folds (Fig. 1F), accompanied by a substantially improved quantum yield ($\Phi_{fl} = 0.555$). To this end, **NCBP** was selected as the optimal candidate sensor based on its superior NIR emission characteristics and high SNR.

3.3. Sensing performance of NCBP for HSA

Next, the TICT behaviors of **NCBP** were verified by its environmental sensitivity (viscosity and solvent polarity) (Pivovarenko and Klymchenko, 2024). In a water-glycerol system, a gradual increase in glycerol content led to a pronounced fluorescence enhancement, owing to the increased viscosity, which promoted molecular coplanarity and favored radiative transitions (Fig. 2A). A similar trend was observed in 1, 4-dioxane–water systems with varying proportions (Fig. 2B). Moreover, polar solvents could strongly induce the TICT state of **NCBP**, resulting in a marked red-shift emission (Fig. 2C and Fig. S24) (Ludwanowski et al., 2021). These results demonstrate that HSA binding can effectively block the TICT process through the conformation rigidification of dyes, thereby enhancing the brightness. Under physiological conditions, **NCBP** could rapidly bind HSA within seconds, forming a stable complex with excellent photostability (Fig. S25–26). A linear fluorescence response was obtained over the HSA concentration range of 0–700 μg/mL, with a limit of detection (LOD) as low as 0.51 μg/mL (Fig. 2D and E). Importantly, **NCBP** exhibited high selectivity for bovine serum albumin (BSA) and HSA, exceeding α-acid glycoprotein (AAG, another high-abundance serum protein) and other proteins (Fig. 2F). These results suggest that **NCBP** is a promising optical tool for the reliable and specific detection of HSA.

3.4. Binding features of NCBP towards HSA

To elucidate the responsive mechanism of **NCBP**, we examined its binding properties with HSA. Fluorescence quenching assays verified the formation of the protein-sensor complex (Fig. 2G and Fig. S27). Gradual addition of increasing concentrations of **NCBP** led to a pronounced quenching of the intrinsic fluorescence of HSA. The calculated

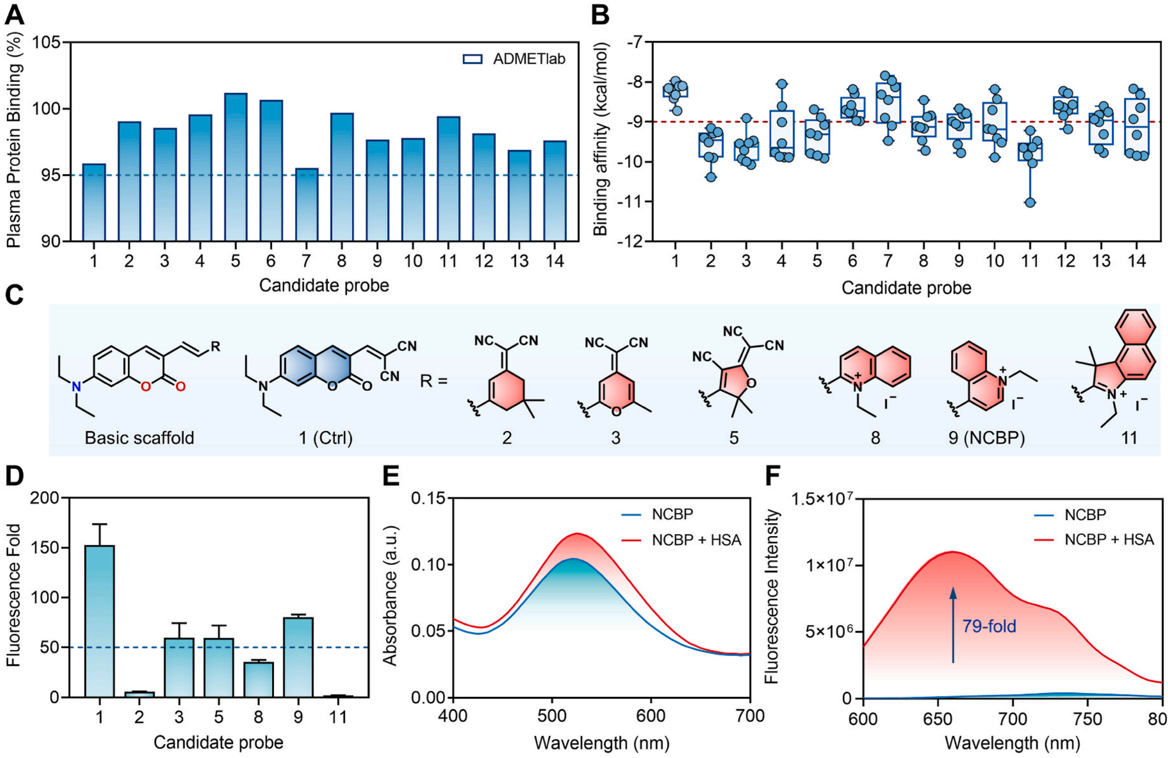

Fig. 1. Optimization of a coumarin-type NIR sensors for light-up sensing HSA. (A) Plasma protein binding rates of candidate sensors using ADMETlab. (B) Binding affinity of candidate sensors for HSA through ensemble docking. (C) Chemical structures of seven sensors. (D) Fluorescence enhancement folds before and after adding HSA. (E–F) Spectroscopic variations in absorption (E) and emission spectra (F) of **NCBP** (10 μM) in the presence or absence of HSA (10 μM).

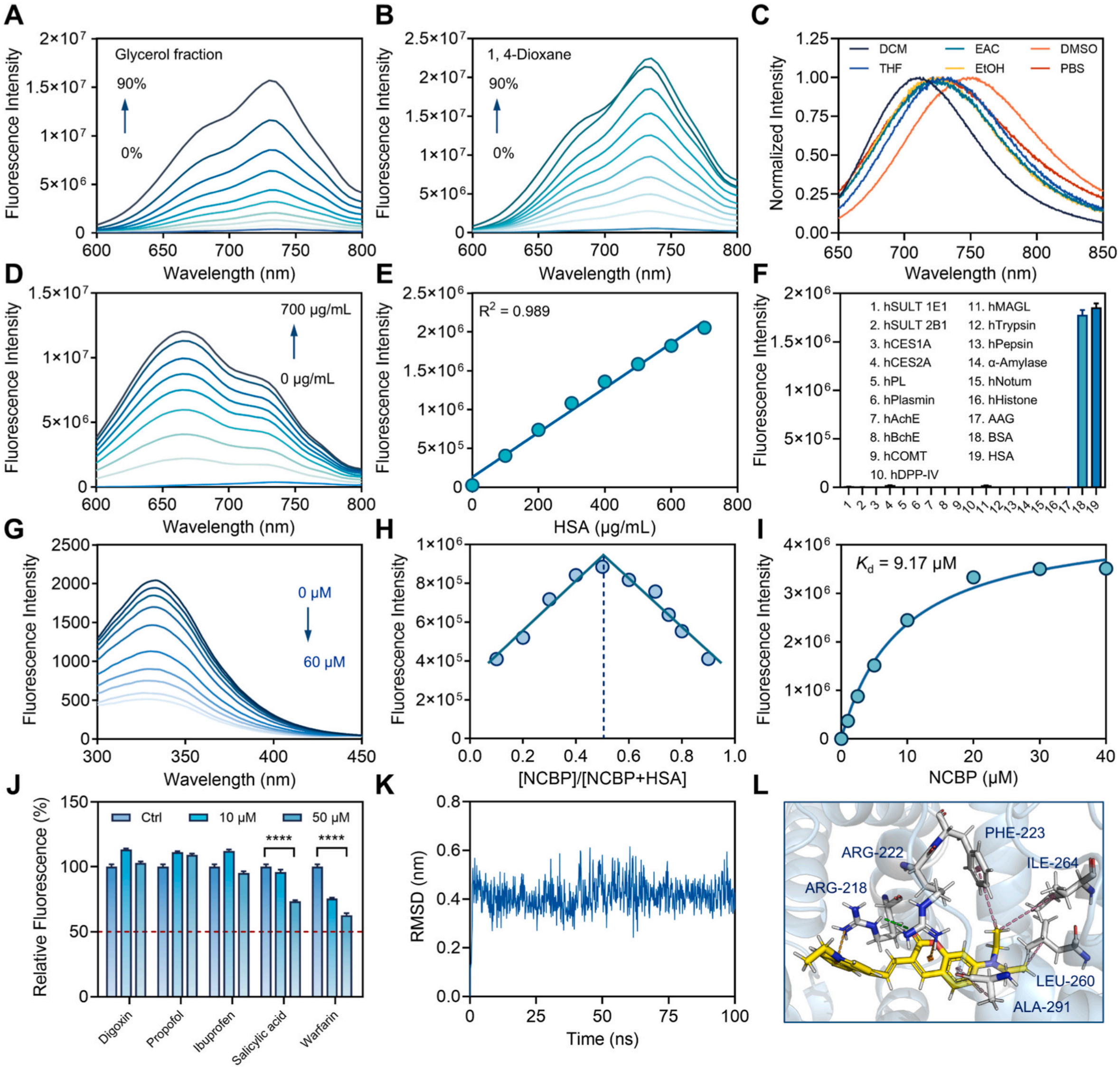

Fig. 2. Sensing performance and binding behaviors of **NCBP** for HSA. (A) Viscosity-dependent fluorescence of **NCBP** (10 μM) in a glycerin-water system. (B) Emission spectra of **NCBP** (10 μM) in a mixture of 1,4-dioxane-water system. (C) Normalized emission spectra of **NCBP** (10 μM) in various solvents. (D) Fluorescence spectra of **NCBP** (10 μM) with increasing HSA concentrations. (E) Quantitative curve of HSA. (F) Selectivity assays of **NCBP**. (G) Fluorescence spectra of HSA in the absence and presence of **NCBP**. (H) Job's plot analysis of fluorescence intensity at 665 nm against [**NCBP**]/([**NCBP**] + [HSA]). (I) Binding kinetics of **NCBP** for HSA. (J) Displacement assays of **NCBP**-HSA complex by site-specific drugs. (K) Root mean square deviation (RMSD) analysis of **NCBP** in HSA (PDB ID: 2BXD). (L) Binding mode of **NCBP** in HSA.

K_{sv} and K_q values were 4.94×10^5 L mol^{-1} and 4.94×10^{13} L mol^{-1} s^{-1}, respectively. The K_q value significantly exceeded the maximum scatter collision quenching constant (2.0×10^{10} L mol^{-1} s^{-1}), indicating that **NCBP** could be tightly captured by HSA (Fan et al., 2023a). Job's plot analysis further revealed that the fluorescence intensity reached a maximum when the molar fraction of **NCBP** reached about 1/2, suggesting that the complex formation followed a 1:1 stoichiometry (Fig. 2H). Furthermore, **NCBP** displayed a desirable affinity, with a dissociation constant (K_d) of 9.17 μM (Fig. 2I). To identify the specific binding site of **NCBP** on HSA, drug competition assays were performed using site-specific drugs, including warfarin (subdomain IIA), salicylic acid (subdomain IIA & IB), ibuprofen (subdomain IIIA), digoxin (subdomain IIIA), and propofol (subdomain IIIA & IIIB) (Czub et al., 2020). Among them, warfarin and salicylic acid reduced the fluorescence signal in a concentration-dependent manner (Fig. 2J), with displacement rates of 37.2% and 26.5%, respectively. Common therapeutic agents and endogenous substances showed negligible interference with the **NCBP**-HSA signal (Fig. S28–29). These results suggest that **NCBP** tightly bind to HSA at the drug-binding site I, with desirable affinity and superior anti-interference ability.

3.5. Binding mode of NCBP in HSA

Meanwhile, molecular dynamics were performed to gain insight into the binding pose of **NCBP** in HSA. The fluctuation in RMSD values of **NCBP** was within 5 Å over a 100 ns simulation period (Fig. 2K). The slight conformation changes suggested that **NCBP** could stably occupy the subdomain IIA of HSA (Fig. S30). Hydrophobic interactions were the primary binding driving force (Fig. 2L and Fig. S31). Notably, the coumarin scaffold could generate π−cation interactions and π−Alkyl interactions. Especially, the lactone structure formed a conventional hydrogen bond with Arg-218. Furthermore, π−Alkyl and Alkyl interactions occurred among the diethylamino moiety and several residues. These interactions indicated that the coumarin ring displayed a high affinity for HSA, which was highly consistent with the warfarin-HSA interaction analysis. The quinoline moiety participated in a

π−cation interaction involving Arg-222. These interactions collectively restricted a geometric twist between the electron donor and acceptor pair, thereby blocking the TICT process and enhancing fluorescent brightness (Wang et al., 2021).

3.6. *Visualization of HSA uptake in living nephrocytes*

The kidney, particularly the proximal tubule, is the primary site for protein reabsorption. As such, the ability of albumin internalization serves as a critical indicator of renal function and a valuable metric for assessing drug-induced nephrotoxicity or nephroprotection. To assess the applicability of **NCBP** in renal function evaluation, a CDDP-induced nephrotoxicity (CINT) model was established. CCK-8 assays revealed the excellent biocompatibility of **NCBP** in both RPTEC and HK-2 cells at concentrations up to 1 μM (Fig. S32). SwissADME calculated key physicochemical properties of **NCBP**, with a lipophilicity (log *P*) of 4.25 and topological polar surface area (tPSA) of 37.33 Å^2. These properties suggested that **NCBP** may possess favorable membrane permeability, with the utility for intracellular imaging. In comparison with the sensor alone, normal RPTEC and HK-2 cells incubated with the HSA-**NCBP** complex exhibited intense red fluorescence, indicating robust albumin uptake (Fig. 3A and D and Fig. S33). Moreover, the dynamic cellular uptake of the **NCBP**-HSA complex was monitored. The results showed that the intracellular fluorescence signal gradually increases within 4 h (Fig. S34). The 1-h incubation time lies within the linear phase, ensuring that the fluorescence signal is proportional to HSA uptake and avoiding saturation or non-linear response regions. Therefore, 1 h co-incubation was used for nephroprotective drug screening. Notably, the cellular red fluorescence signal was markedly diminished in CDDP-challenged nephrocytes, suggesting severe impairment of reabsorption function (Fig. 3C and F). This severe damage was further verified by enhanced green fluorescence, which signified intracellular ROS accumulation resulting from CDDP-induced oxidative stress (Fig. 3B and E). Sulforaphane (SFN), a known Nrf2 activator, has been established as a classic nephroprotective agent against CDDP-induced renal injury (Deng et al., 2025). As expected, SFN led to a dose-dependent recovery of red fluorescence, indicating restored albumin uptake, alongside a concurrent reduction in intracellular ROS. These findings demonstrate that **NCBP** can effectively assess drug-induced nephrotoxicity and identify renal protective drugs through real-time visualization of albumin endocytosis.

3.7. *Discovery of nephroprotective drugs against CINT*

In the course of drug development, natural compounds demonstrate inherent antioxidant, anti-inflammatory, and anti-apoptotic properties, with significant therapeutic potential in ameliorating CINT (Fang et al.,

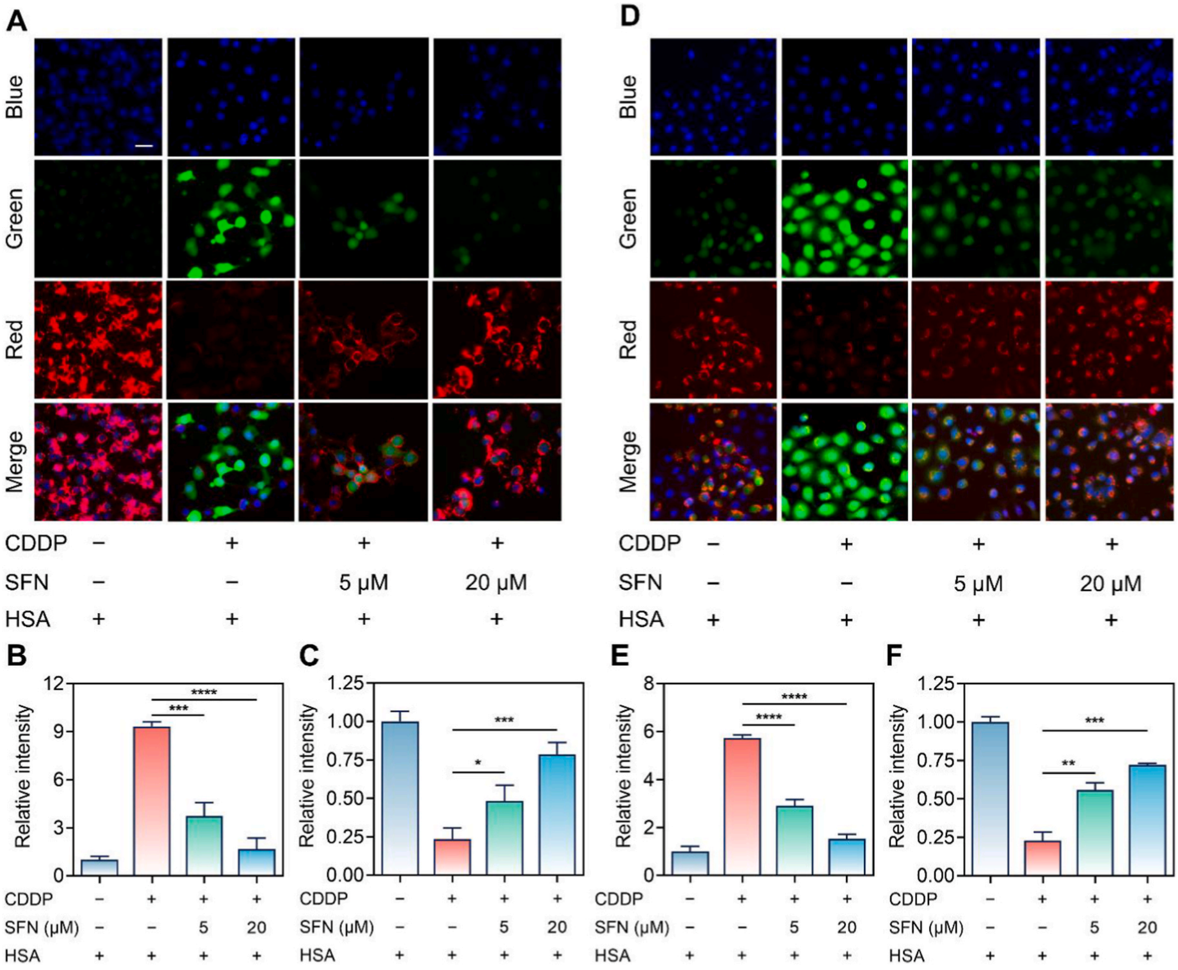

Fig. 3. *In-situ* imaging of HSA endocytosis for evaluating the nephroprotective effects of SFN against CDDP-induced nephrocyte injury. (A, D) Fluorescence imaging of HSA internalization (red fluorescence) and intracellular ROS accumulation (green fluorescence) in RPTEC (A) and HK-2 cells (D). Cells were pretreated with Hoechst 33,342, DCFH-DA, and **NCBP** for 30 min and followed by addition of DMSO (Ctrl group), CDDP alone, or CDDP combined with different doses of SFN (5 μM, 20 μM), respectively. Scale bar: 25 μm. (B−C) Quantitative analysis of intracellular ROS levels (B) and HSA endocytosis efficiency (C) in RPTEC cells. $^{*}P < 0.05$, $^{**}P < 0.01$, $^{***}P < 0.001$, $^{****}P < 0.0001$. (E−F) Quantitative analysis of intracellular ROS levels (E) and HSA endocytosis efficiency (F) in HK-2 cells. (For interpretation of the references to colour in this figure legend, the reader is referred to the Web version of this article.)

2021). A series of natural flavonoids, chalcones, and their derivatives was preliminarily evaluated for nephroprotective activity against CINT (Fig. 4A and Table S4). Notably, several candidates at 10 μM exhibited varying degrees of enhanced albumin internalization (Fig. 4B). Among them, nobiletin (NOB) and 4',7-dimethoxyisoflavone (DIF) emerged as two promising lead compounds, exhibiting low cytotoxicity and superior efficacy over SFN in restoring impaired albumin endocytosis after CDDP injury (Fig. 4B–D). Fluorescence imaging further revealed that pretreatment with NOB or DIF effectively attenuated the **NCBP**-HSA uptake and concurrently suppressed intracellular ROS accumulation in a dose-dependent manner (Fig. 4E–J). These findings align with previous evidence that NOB suppresses apoptotic pathway activation and DNA damage, thereby ameliorating CINT (Malik et al., 2015). Importantly, DIF was identified for the first time as a novel nephroprotective drugs against CINT, validating the utility of albumin reabsorption-based phenotypic platform in discovering novel nephroprotective agents.

3.8. *Nephroprotective effects of NOB and DIF*

The nephroprotective effects of NOB and DIF were investigated in a mouse model of CDDP-induced kidney injury (CIKI) (Fig. 5A). In the CDDP-treated group, the kidney tissues exhibited pronounced pallor and edema, accompanied by severe histopathological alterations, including tubular dilation and tubular epithelial cell necrosis (Fig. 5B). Pretreatment with NOB or DIF markedly improved renal appearance and attenuated these histopathological lesions, with 40 mg/kg showing the most pronounced nephroprotective effects. Body weight was markedly reduced in CIKI mice at 72 h post-injection, whereas NOB and DIF effectively prevented weight loss across all tested doses (Fig. 5C). Serum biochemical analysis further demonstrated that CDDP significantly elevated the levels of BUN, CREA, AST and ALT, while NOB or DIF treatment reversed them to the normal states (Fig. 5D–G). H&E and PAS staining confirmed that NOB and DIF alleviated tubular injury,

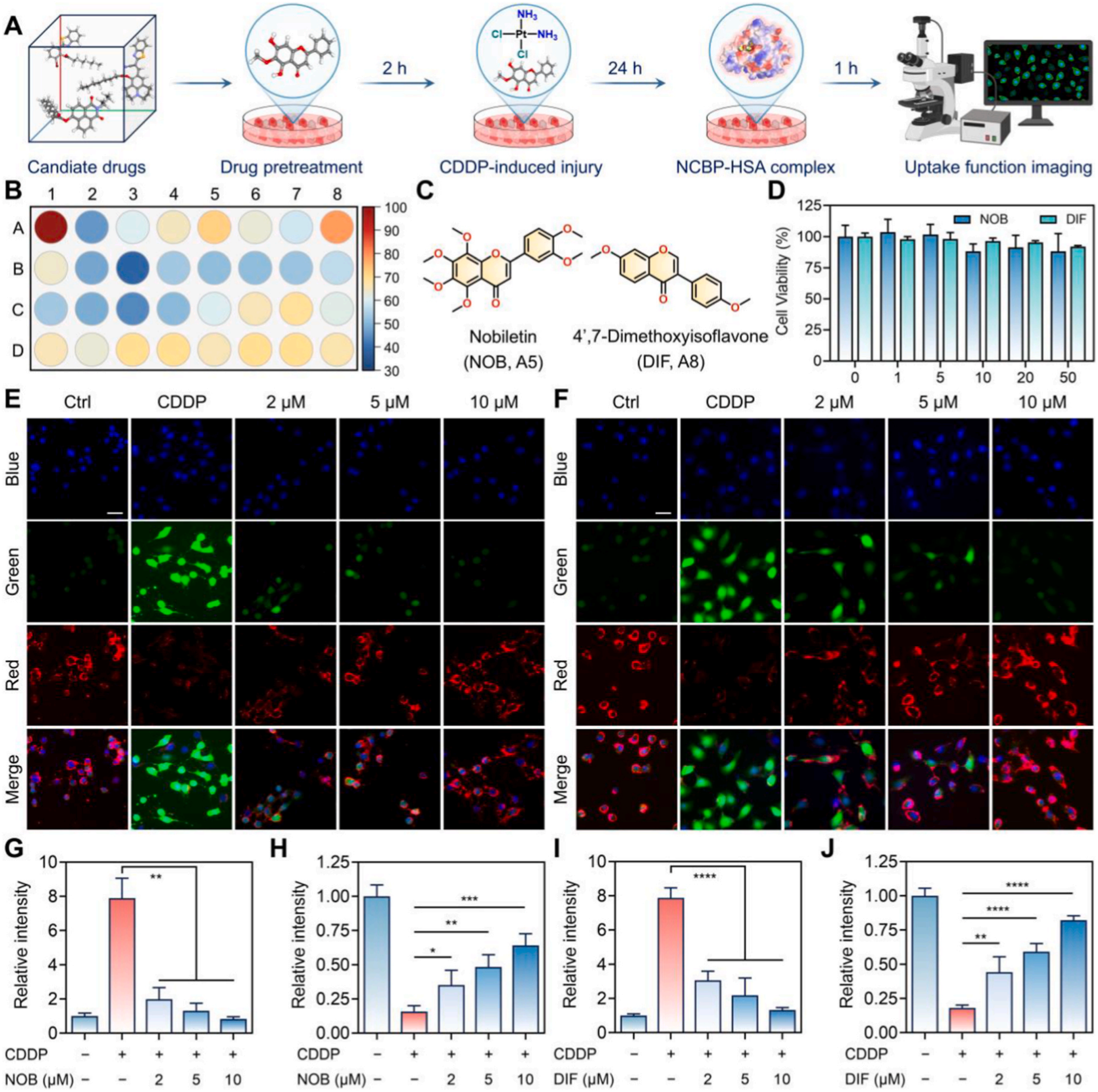

Fig. 4. Visual screening of nephroprotective agents. (A) Experimental scheme for assessing nephroprotective effects of natural products and their derivatives using albumin uptake as a pharmacological phenotype. (B) Relieving capacity of natural products and derivatives (10 μM) against CINT in RPTEC cells. Note: A1, Ctrl group (DMSO only); A2, CDDP treatment group; A3, positive drug group (SFN). (C) Chemical structures of nobiletin (NOB, A5) and 4′,7-dimethoxyisoflavone (DIF, A8). (D) Cytotoxicity of NOB and DIF in RPTEC cells for 24 h. (E–F) Fluorescence imaging of the uptake of **NCBP**-HSA complex in RPTEC cells pretreated with NOB (E) and DIF (F). Scale bar: 25 μm. (G–H) Quantification of albumin uptake (E) and ROS levels (F) upon addition of NOB. (I–J) Quantification of albumin uptake (I) and ROS levels (J) upon addition of DIF. **P* < 0.05, ***P* < 0.01, ****P* < 0.001, *****P* < 0.0001.

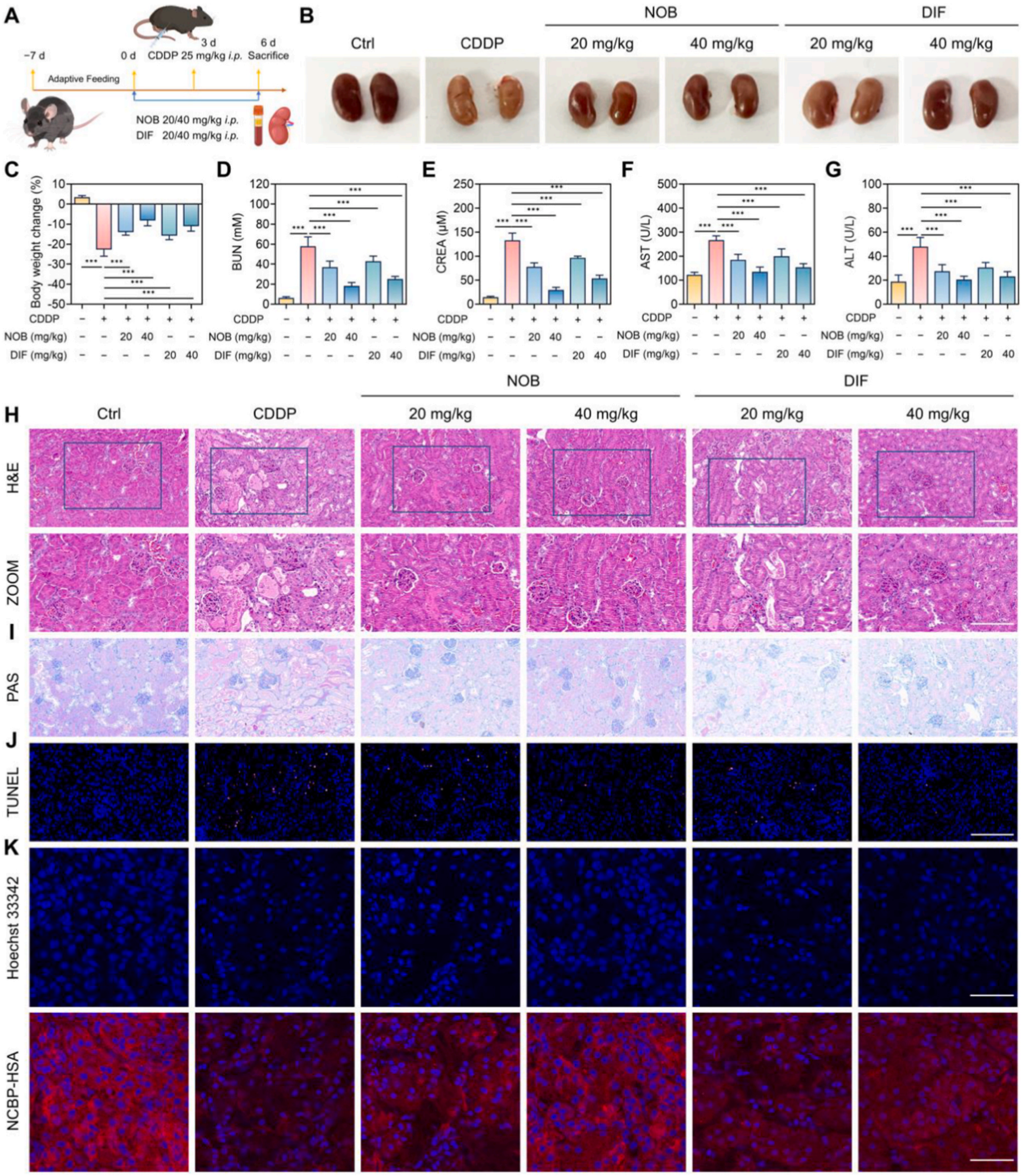

Fig. 5. Nephroprotective effects of NOB and DIF in a CIKI mouse model. (A) Experimental design timeline. (B) Representative gross morphology of kidney. (C) Body weight of mice. (D–G) Serum biochemical parameters, including BUN (D), CREA (E), AST (F), and ALT (G). Data are expressed as mean ± SD; statistical significance was evaluated by one-way ANOVA. ***$P < 0.001$. (H–I) Histological analysis of kidney sections using H&E (H) and PAS (I) staining (n = 6, scale bar = 100 μm). (J) TUNEL assay of kidney sections (n = 6, scale bar = 100 μm). (K) Visualization of the reuptake ability of renal tissue for the **NCBP**-HSA complex. Scale bar = 50 μm.

evidenced by reduced tubular swelling, vacuolar degeneration, epithelial cell detachment, necrosis, and cast formation (Fig. 5H and I). Given that apoptosis is a hallmark of CIKI, TUNEL staining was performed to assess tubular cell apoptosis. CDDP significantly increased the number of TUNEL-positive cells, whereas NOB or DIF treatment markedly attenuated apoptotic cell death (Fig. 5J). Reabsorption imaging of **NCBP**-HSA in renal tissues provided direct visual evidence of the functional efficacy of NOB and DIF in mitigating CIKI at the organ level (Fig. 5K and Fig. S35). Collectively, these results demonstrate that NOB and DIF effectively mitigate CIKI *in vivo*.

4. Conclusion

In summary, inspired by warfarin's high affinity for HSA, a library of coumarin-based TICT sensors was rationally constructed. Through affinity prediction and fluorescence screening, **NCBP** was identified as the optimal sensor for light-up sensing HSA. Compared with previous HSA sensors, **NCBP** integrated NIR emission, high quantum yield, ultrahigh sensitivity (LOD = 0.51 μg/mL), rapid response, and excellent selectivity. Its remarkable fluorescence enhancement, strong binding affinity, and suitable kinetic performance ensure high-contrast and prolonged imaging under physiological conditions. We further applied **NCBP** to evaluate HSA uptake in different renal cell types, establishing a phenotypic platform for assessing renal function. The natural products NOB and DIF were recognized as nephroprotective agents that restored renal uptake function and alleviated oxidative stress *in vitro* and *in vivo*. Collectively, this study devised an easy-to-use NIR tool for real-time mapping of cellular HSA uptake and offered a phenotypic platform for assessing drug-induced nephrotoxicity and discovering nephroprotective agents, advancing research in chemical biology, pharmacology, and nephrology.

CRediT authorship contribution statement

Yufan Fan: Data curation, Formal analysis, Investigation, Methodology, Software, Writing – original draft. **Bei Zhao:** Formal analysis, Methodology, Writing – original draft. **Ya Zhang:** Data curation, Methodology, Writing – original draft. **Pingjin Xie:** Methodology. **Lele Liu:** Methodology. **Xuerui Wang:** Methodology. **Guanghao Zhu:** Methodology. **Zhaobin Guo:** Methodology. **Fangyuan Wang:** Formal analysis, Methodology, Writing – review & editing. **Qiang Jin:** Formal analysis, Methodology, Writing – review & editing. **Jing Hu:** Formal analysis, Funding acquisition, Project administration, Supervision, Writing – review & editing. **Guangbo Ge:** Formal analysis, Funding acquisition, Project administration, Supervision, Writing – review & editing.

Declaration of competing interest

The authors declare that they have no competing financial interests or personal relationships that could have appeared to influence the work reported in this paper.

Acknowledgment

This work was supported by National Key Research and Development Program of China (2022YFC3502000), Noncommunicable Chronic Diseases-National Science and Technology Major Project (2025ZD0546900), the NSF of China (U23A20516, 82304446, 82474023, 82404925, and 82204592), Shanghai Sailing Program (23YF1442700), Shenzhen Medical Research Fund (C2501037), Scientific Research Project of Shenzhen Society of Traditional Chinese Medicine (2024060F), 2025 Shantou Fine Chemical Enterprises Introducing Scientific and Technological Leading Talent Team and Import Substitution Tackling Special Funds Project (STKJ2025046), and China Postdoctoral Science Foundation (2025M783937). We thank the staff members of the Integrated Laser Microscopy System at the National Facility for Protein Science in Shanghai, for providing technical support and assistance in data collection and analysis.

Appendix A. Supplementary data

Supplementary data to this article can be found online at https://doi.org/10.1016/j.bios.2026.118490.

Data availability

The authors do not have permission to share data.

References

Arques, S., 2018. Eur. J. Intern. Med. 52, 8–12.
Carvalho, J.R., Verdelho Machado, M., 2018. Ann. Hepatology 17 (4), 547–560.
Chen, Q., Fang, H., Shao, X., Tian, Z., Geng, S., Zhang, Y., Fan, H., Xiang, P., Zhang, J., Tian, X., Zhang, K., He, W., Guo, Z., Diao, J., 2020. Nat. Commun. 11 (1), 6290.
Czub, M.P., Handing, K.B., Venkataramany, B.S., Cooper, D.R., Shabalin, I.G., Minor, W., 2020. J. Med. Chem. 63 (13), 6847–6862.
Deng, Y., Xu, L., Jiang, Z., Chen, L., Zhu, G., Xu, C., Chu, X., Wang, L., Niu, X., Chen, L., Xiao, Z., Hu, J., Ge, G., 2025. Redox Biol. 85, 103737.
Fan, Y., Wang, F., Hou, F., Wei, L., Zhu, G., Zhao, D., Hu, Q., Lei, T., Yang, L., Wang, P., Ge, G., 2023a. Chin. Chem. Lett. 34 (2).
Fan, Y., Wu, Y., Hou, J., Wang, P., Peng, X., Ge, G., 2023b. Coord. Chem. Rev. 480, 215020.
Fan, Y., Zhang, F., Hao, Y., Chen, L., Zhou, Q., Zeng, H., Song, Y., Guo, Z., Peng, X., Ge, G., 2025. Adv. Funct. Mater. 35, 2416057.
Fan, Y., Zhang, T., Song, Y., Sang, Z., Zeng, H., Liu, P., Wang, P., Ge, G., 2023c. Anal. Chem. 95 (42), 15665–15672.
Fang, C.Y., Lou, D.Y., Zhou, L.Q., Wang, J.C., Yang, B., He, Q.J., Wang, J.J., Weng, Q.J., 2021. Acta Pharmacol. Sin. 42 (12), 1951–1969.
Fu, M., Sun, Y., Kenry, Zhang, M., Zhou, H., Shen, W., Hu, Y., Zhu, Q., 2021. Chem. Commun. (Camb) 57 (28), 3508–3511.
Gao, D., Li, Y., Wu, Y., Liu, Y., Hu, D., Liang, S., Liao, J., Pan, M., Zhang, P., Li, K., Liu, X., Zheng, H., Sheng, Z., 2023. ACS Appl. Mater. Interfaces 15 (1), 3–13.
Gao, S., Wei, G., Zhang, S., Zheng, B., Xu, J., Chen, G., Li, M., Song, S., Fu, W., Xiao, Z., Lu, W., 2019. Nat. Commun. 10 (1), 2206.
Ge, G.B., Feng, L., Jin, Q., Wang, Y.R., Liu, Z.M., Zhu, X.Y., Wang, P., Hou, J., Cui, J.N., Yang, L., 2017. Anal. Chim. Acta 989, 71–79.
Ghuman, J., Zunszain, P.A., Petitpas, I., Bhattacharya, A.A., Otagiri, M., Curry, S., 2005. J. Mol. Biol. 353 (1), 38–52.
Gu, H., Wang, W., Wu, W., Wang, M., Liu, Y., Jiao, Y., Wang, F., Wang, F., Chen, X., 2023. Chem. Commun. (Camb) 59 (15), 2056–2071.
Guo, R., Ma, Y., Tang, Y., Xie, P., Wang, Q., Lin, W., 2019. Talanta 204, 868–874.
Jin, Q., Feng, L., Zhang, S.J., Wang, D.D., Wang, F.J., Zhang, Y., Cui, J.N., Guo, W.Z., Ge, G.B., Yang, L., 2017. Anal. Chem. 89 (18), 9884–9891.
Kim, S.J., Rhee, H.W., Park, H.J., Kim, H.Y., Kim, H.S., Hong, J.I., 2013. Bioorg. Med. Chem. Lett. 23 (7), 2093–2097.
Kumar, D., Banerjee, D., 2017. Clin. Chim. Acta 469, 150–160.
Liu, L., Fan, Y., Lin, H., Lei, J., Guo, J., Chen, L., Xiao, Z., Song, Y., Yang, X., Ge, G., Tang, H., 2025. Sens. Actuators, B 431, 137427.
Ludwanowski, S., Samanta, A., Loescher, S., Barner-Kowollik, C., Walther, A., 2021. Adv. Sci. (Weinh) 8 (5), 2003740.
Malik, S., Bhatia, J., Suchal, K., Gamad, N., Dinda, A.K., Gupta, Y.K., Arya, D.S., 2015. Exp. Toxicol. Pathol. 67 (7-8), 427–433.
Niu, X., Fan, Y., Chen, L., Deng, Y., Hao, Y., Zhu, G., Wang, L., Zhou, Q., Zhu, G., Ge, G., 2026. Chin. Chem. Lett. 37, 111204.
Niu, X., Fan, Y., Zhu, G., Zeng, H., Zhao, B., Sun, M., Chen, L., Wu, L., Tian, Z., James, T. D., Ge, G., 2025. Biosens. Bioelectron. 275, 117192.
Pivovarenko, V.G., Klymchenko, A.S., 2024. Chem. Rec. 24 (2), e202300321.
Sedgwick, A.C., Wu, L., Han, H.H., Bull, S.D., He, X.P., James, T.D., Sessler, J.L., Tang, B. Z., Tian, H., Yoon, J., 2018. Chem. Soc. Rev. 47 (23), 8842–8880.
Song, L., Sun, M., Song, Y., Zhang, F., Zhao, B., Zeng, H., Shi, J., Liu, H., Zhao, S., Tian, T., Yin, H., Ge, G., 2024. Chin. Chem. Lett. 35 (11), 109601.
Song, Y., Zhang, F., Guo, J., Fan, Y., Zeng, H., Sun, M., Qian, J., Qi, S., Chen, Z., Jin, X., Song, Y., Tian, T., Qian, Z., Sun, Y., Tian, Z., Yu, B., Ge, G., 2025. Acta Pharm. Sin. B 15 (8), 4174–4192.
Strauss, C., Booke, H., Forni, L., Zarbock, A., 2024. J. Clin. Anesth. 95, 111458.
Sun, Q., He, D., Zhang, L., Li, Z., Qu, L., Sun, Y., 2023. TrAC, Trends Anal. Chem. 167.
Tang, C., Livingston, M.J., Safirstein, R., Dong, Z., 2023. Nat. Rev. Nephrol. 19 (1), 53–72.
Tu, Y., Yu, Y., Zhou, Z., Xie, S., Yao, B., Guan, S., Situ, B., Liu, Y., Kwok, R.T.K., Lam, J.W. Y., Chen, S., Huang, X., Zeng, Z., Tang, B.Z., 2019. ACS Appl. Mater. Interfaces 11 (33), 29619–29629.
Ufer, M., 2005. Clin. Pharmacokinet. 44 (12), 1227–1246.
Wang, C., Chi, W., Qiao, Q., Tan, D., Xu, Z., Liu, X., 2021. Chem. Soc. Rev. 50 (22), 12656–12678.
Wang, H., Wang, J., Ma, G., Zhou, J., Du, L., Wu, H., Zhang, X., He, Y., Zhou, J., 2023. Chem. Eng. J. 464, 142551.
Wang, Y.-R., Feng, L., Xu, L., Hou, J., Jin, Q., Zhou, N., Lin, Y., Cui, J.-N., Ge, G.-B., 2017. Sens. Actuators, B 245, 923–931.
Wen, Y., Parikh, C.R., 2021. Crit. Rev. Clin. Lab Sci. 58 (5), 354–368.
Xing, P., Niu, Y., Mu, R., Wang, Z., Xie, D., Li, H., Dong, L., Wang, C., 2020. Nat. Commun. 11 (1), 1573.
Xu, J.F., Yang, Y.S., Jiang, A.Q., Zhu, H.L., 2022. Crit. Rev. Anal. Chem. 52 (1), 72–92.
Yang, H., Chen, Y., He, J., Li, Y., Feng, Y., 2025. BMC Nephrol. 26 (1), 115.
Yang, Y., He, L., Lin, W., 2020. J. Photochem. Photobiol., A 401, 112789.
Zhu, Z., Chen, X., Liao, H., Li, L., Yang, H., Wang, Q., Zhu, W.H., 2024. Aggregate 5 (3), e526.